Research Paper

Metal-free black phosphorus nanosheets-decorated graphitic carbon nitride nanosheets with C−P bonds for excellent photocatalytic nitrogen fixation

Pengxiang Qiu[1], Chenmin Xu[1], Ning Zhou, Huan Chen[*], Fang Jiang[*]

Key Laboratory of Jiangsu Province for Chemical Pollution Control and Resources Reuse, School of Environmental and Biological Engineering, Nanjing University of Science and Technology, Nanjing 210094, China

ARTICLE INFO

ABSTRACT

Visible light photocatalytic nitrogen fixation, as a low-cost and mild technology, needs efforts to explore an economical photocatalyst with high activity and stability. In this study, a metal-free black phosphorus (BP) nanosheets-decorated graphitic carbon nitride nanosheets photocatalyst (BPCNS) has been successfully synthesized. With BP acting as the cocatalyst, BPCNS shows excellent performance in both visible light nitrogen photofixation and pollutant reduction owing to the increased number of excited electrons and enhanced separation efficiency of charge carriers through formation of C−P covalent bonds. Besides, the chemical structure of the BPCNS with optimal content of BP remains the same after exposure to air for 30 days or after five cycles of photocatalytic nitrogen fixation, since the occupation of the lone pairs on phosphorus atoms largely improves the chemical stability of BP.

1. Introduction

Nitrogen fixation is one of the most important reactions in nature since nitrogen (N) is a critical element in building biomolecules [1]. The Haber–Bosch process is used for nitrogen fixation in the industry; however, the Haber–Bosch process needs to consume a large amount of energy due to the harsh reaction condition (300–500 °C and 15–25 MPa) [2]. Therefore, an environmentally friendly method with low energy consumption for nitrogen fixation is highly required. Photocatalysis has great potential in nitrogen fixation as a green and economical technology with solar energy being the driving force in the reaction process [3].

Graphitic carbon nitride (CN), an organic polymeric semiconductor, is regarded as one of the most promising photocatalysts [4]. CN has the advantages of rich raw material, low cost, simple synthesis and visible light response [5], while it also suffers from the limited carrier separation efficiency and limited specific surface area [6]. Exfoliation is an effective method to enhance the catalytic performance of CN. The graphitic carbon nitride nanosheets (CNS) exhibit superior photoelectrical properties on account of large surface area and shortened charger carriers transferring distance [7]. The modification of CN with a cocatalyst, such as Au [8], Ag [9], Pt [10], Pd [11], and their oxides, is another strategy to improve the photocatalytic activity. Though these precious metals show high performance in cocatalysis, their application

is limited by high price and low reserves. Thus, it is a prominent challenge to find cheap cocatalyst with high reserves in the nature. Several metal-free cocatalyst/CN systems have been reported recently with carbon based material (such as carbon quantum dots [12], graphene oxide [13], carbon nanotubes [14] and C_{60} [15]) as the cocatalyst, while cotacalyst made of other nonmetallic elements are rarely reported.

Phosphorus (P) is one of the most abundant elements on earth. There are several kinds of P allotropes, including white, red and black phosphorus, among which black phosphorus (BP) is the most stable one [16]. Tunable band gap (0.3–2 eV) and high charge-carrier mobility $(1000\ cm^2\ V^{-1}\ s^{-1})$ [17] make BP a promising candidate for field-effect transistor [18], lithium battery [19], gas sensor [20], thermoelectric devices [21], super capacitor [22], and et al. However, there has been limited reports introducing BP as a photocatalyst for the oxidation of organic pollutant [23,24], and to the best of our knowledge no research about BP as a cocatalyst has been published so far. In addition, the formation of bonding state between cocatalyst and photocatalyst has not been paid with enough attention. Wu et al. reported the (Co, Fe) −N−C as the active sites for oxygen reduction reaction (ORR) [25]. Recently, Li et al. reported the enhancement of P−Co−N in CoP/ CN to photocatalytic hydrogen evolution [26]. The effect of C−P bond between cocatalyst and CN to the catalytic system has not been reported yet. There are ample functional groups on the surface of CNS,

which is theoretically possible to react with the lone pair electrons of BP to form C−P bonds.

Herein, we synthesized metal-free black phosphorus nanosheets/graphitic carbon nitride nanosheets photocatalyst (BPCNS) with stable C−P bond through a post calcination process for the first time. BPCNS shows remarkably enhanced photocatalytic nitrogen fixation efficiency compared with CNS and Pt/CNS. Besides, we report the effect of C−P in BPCNS on stability and catalytic efficiency for the first time.

2. Experimental section

2.1. Synthesis of BPCNS

Bulk BP was synthesized via a facile low-pressure transport route according to the literature [27]. In a typical synthesis, 500 mg of red phosphorus (99.999%, Aladdin), 10 mg of SnI₄ (99.999%, Sigma–Aldrich), and 20 mg of Sn (99.998%, Sigma–Aldrich) were sealed in a quartz tube under vacuum. The quartz tube was heated up to 923 K at a heating rate of 1.35 K per minute. After keeping at 923 K for five hours, the temperature was reduced to 773 K at a cooling rate of 0.33 K per minute followed by a natural cooling process. The large BP crystals were then carefully collected and kept in a glove box for further use.

The bulk CN was synthesized by direct heating of dicyandiamide (99.5%, TCI) at 823 K for 4 h.

The black phosphorus nanosheets (BPNS) or CNS were prepared through liquid exfoliation of the corresponding bulk sample. In detail, 30 mg of BP or CN was dispersed in 100 mL of water under argon and the suspension was sonicated for 10 h. The nanosheets were finally obtained by centrifugation of the stable suspension at 5000 rpm for 10 min.

A certain volume of the BPNS suspension (0.3 mg mL⁻¹) was added to 100 mL of a CNS suspension (0.3 mg mL⁻¹) and sonicated for 30 min under argon to obtain a stable homogeneous dispersion of the BPNS and CNS. The dispersion was then centrifuged and dried under vacuum to obtain BPNS/CNS.BPNS/CNS was calcined in argon at 573 K for 2 h to acquire the final product BPCNS. The resulting composite catalyst was denoted as xBPCNS, where x is the mass ratio of BP to CNS. A control sample without calcination was prepared and labeled as 0.05BPCNS-WC.

2.2. Synthesis of Pt-CNS

Pt-CNS was synthesized by a photodeposition method. In detail, 500 mg of CNS, a certain amount of H₂PtCl₆, and 10 mL of methanol were added into a quartz reactor with 200 mL of distilled water. The suspension was stirred for 1 h before a 500 W Hg lamp was turn on. After 5 h irradiation, the product was collected by centrifugation. Then the product was washed several times and dried under 333 K. The final product was labeled as xPt-CNS, where x is the mass ratio of Pt to CNS.

2.3. Characterization

Powder X-ray diffraction (XRD) patterns were recorded on an X-ray diffractometer (Bruker D8 Advance) using Cu Kα (λ = 1.540 Å). Transmission electron microscopy (TEM) images were performed using JEOL JEM2100. Transmission electron microscopy energy dispersive X-ray analysis (TEM-EDX) mapping was acquired on an aberration-corrected transmission electron microscopy (Titan G2 60-300, FEI). Field emission scanning electron microscopy (FESEM) images were observed on Hitachi S-4800 at an accelerating voltage of 15.0 kV. Atomic force microscopy (AFM) images were obtained on Bruker Diension Icon microscope. Nitrogen adsorption-desorption isotherms were measured at 77 K using Micrometritics ASAP 2020. The specific surface area was calculated with the Brunauer–Emmett–Teller (BET) method and the pore size distribution of the sample was calculated from desorption branch isotherms. X-ray photoelectron spectroscopy (XPS) and valence

band X-ray photoelectron spectroscopy (VBXPS) measurements were carried out on ESCALAB 25 (Thermo-VG Scientific). The Fourier transform infrared (FT-IR) experiment was carried out on a Nicoletis10 spectrometer (ThermoFisher). The ³¹P cross-polarization magic angle spinning nuclear magnetic resonance (NMR) spectra were recorded with a Bruker Avance 400 spectrometer at room temperature. UV–vis diffuse reflectance spectroscopy (UV–vis DRS) were obtained on the dry-pressed disk samples using UV–vis spectrometer (Evolution 220, ThermoFisher). Photoluminescence (PL) spectra were measured on a FL3-Tcspc spectroscope (Jobin Yvon). Time-resolved fluorescence decay spectra were obtained with an Edinburgh FLSP920 spectrophotometer with an excitation wavelength of 338 nm. The electron paramagnetic resonance (EPR) measurements were carried out on JES-FA200 (JOEL). Electrical impedance spectroscopy (EIS), linear sweep voltammetry (LSV) and photocurrent transient response were tested with a CHI 660E electrochemical workstation in a standard three-electrode system using the prepared samples as the working electrodes. To prepare the working electrode in LSV experiment, 5 mg of catalyst was mixed with 500 μL of distilled water, 500 μL of ethanol, and 80 μL of 5 wt% Nafion solution with the aid of ultrasonic agitation to form a homogeneous catalyst-Nafion suspension. Then 5 μL of suspension was dropped onto a glassy carbon electrode (GCE) with 3 mm diameter. LSV was performed in 0.5 M Na₂SO₄ solution after 50 cyclic voltammetry (CV) scans with a scan rate of 5 mV s⁻¹. Potential corrections for the iR drop were applied.

2.4. Visible-light photocatalytic reduction of Cr(VI)

The catalyst (20 mg) was added to 50 mL of 10 mg L⁻¹ Cr(VI) solution consisting of 5 mL methanol and 45 mL purified water. The mixture was kept stirring in the dark for 60 min to reach adsorption–desorption equilibrium before a 500 W Xe lamp was turned on. At given time intervals of irradiation, 1 mL of suspension was withdrawn and filtered to remove all catalyst particles. The concentration of Cr(VI) was evaluated with a high-performance liquid chromatograph (e2685, Waters) equipped with a UV–vis detector (2489, Waters). An XBridge C18 column (4.6 × 250 mm) from Waters was adopted for separation using methanol and 5 wt% acetic acid aqueous solution (60/40, V/V) as the mobile phase. The flow rate was 1 mL min⁻¹ and the detection wavelength was 285 nm.

2.5. Visible-light photocatalytic nitrogen fixation

The catalyst (30 mg) was added into 50 mL 5 vol% methanol aqueous solution. Nitrogen was bubbled through at a flow rate of 100 mL min⁻¹. The suspension was stirred for 30 min and then the 500 W Xe lamp with a 420 nm cutoff filter was turned on. At given time intervals of irradiation, 2 mL suspension was collected and centrifuged to obtain liquid samples. The concentration of ammonia was determined using Nessler's reagent.

3. Results and discussion

Fig. 1a compares the XRD patterns of BPCNS samples with varying BP contents (1–10 wt%) with patterns for bulk CN and CNS. The XRD pattern recorded for CN has two distinct diffraction peaks: the strong one at 27.4° indexed for graphitic material as the (002) plane represents the interlayer stacking of the conjugated double bonds. The weak diffraction peak at 13.1° is indexed as (100) in JCPDS 87-1526. The XRD pattern of CNS has two consistent peaks with bulk CN, suggesting that the nanosheets basically have the same crystal structure as their parent CN. However, the peak of CNS at 27.4° becomes less pronounced, suggesting the successful exfoliation of CN [28]. The XRD pattern of pure BP has five discernible diffraction peaks, which confirms the orthorhombic structure of BP according to JCPDS 76-1957 [23]. The BPCNS samples with BP contents of 5 wt% and 10 wt% exhibit
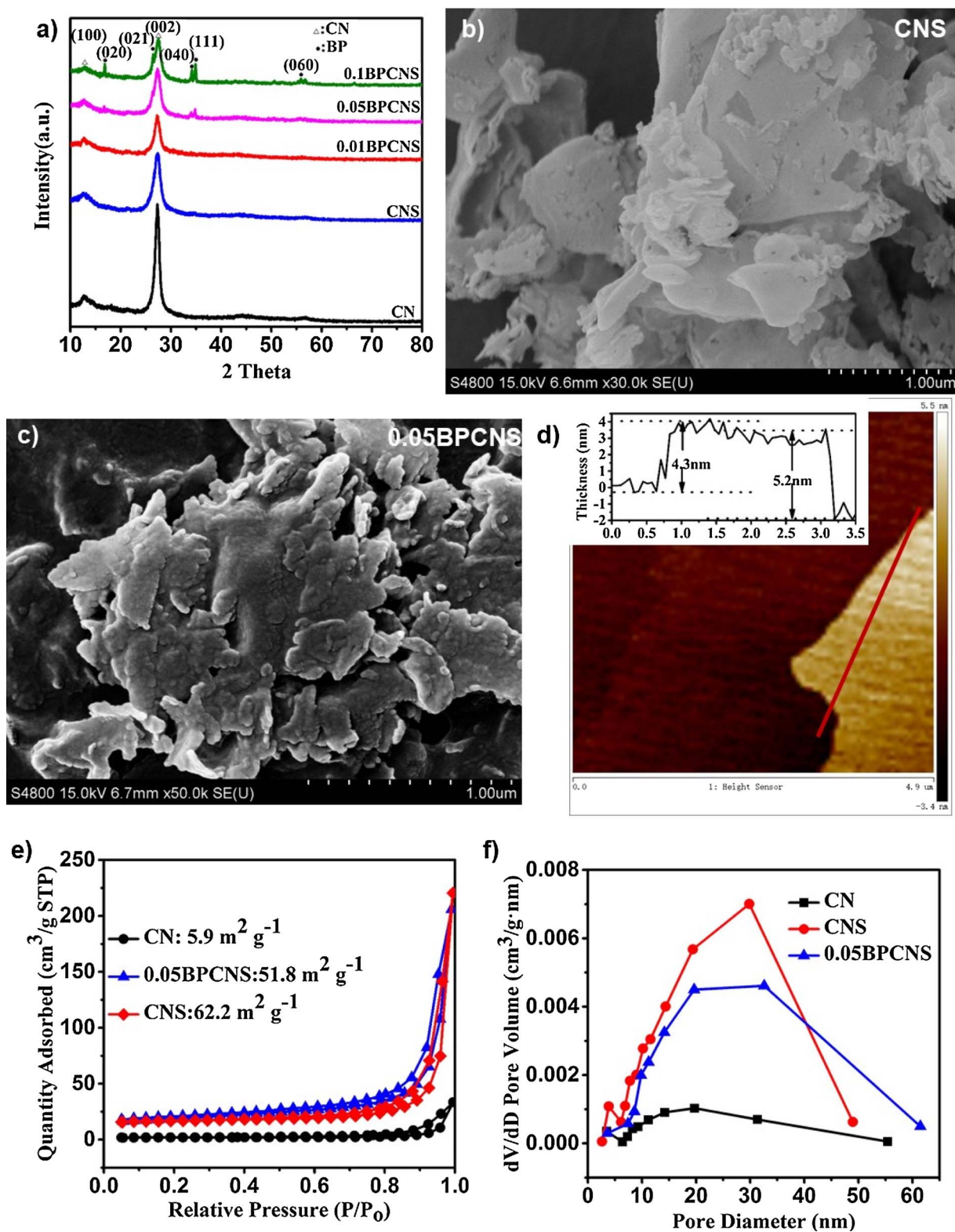
Fig. 1. a) The XRD pattern of CN, CNS, and BPCNS. The FESEM images of b) CNS and c) 0.05BPCNS. d) AFM image of 0.05BPCNS. e) Nitrogen adsorption-desorption isotherms and f) pore size distributions of CN, CNS, and 0.05BPCNS.

diffraction peaks corresponding to both CNS and BP, reflecting of the presence of two phases. Similar XRD patterns are observed for 0.05BPCNS-WC (Fig. S1), suggesting that both BP and CNS exist in 0.05BPCNS-WC. No diffraction peaks assigned to BP can be observed in the XRD patterns of 0.01 BPCNS due to the low amount of BP and high BP dispersion on the surface of CNS. A TEM image of 0.05BPCNS is presented in Fig. S2a. The random distribution of BP on the surface of CNS can be clearly observed. The elemental mappings (Fig. S2b) of C, N, O, and P clearly exhibit the BP are highly dispersed on the surface of CNS after calcination. FESEM images of CNS and 0.05BPCNS were presented in Fig. 1b and c. Compared with CNS, 0.05BPCNS showed a relatively rough surface due to the load of BPNS. Besides, the AFM
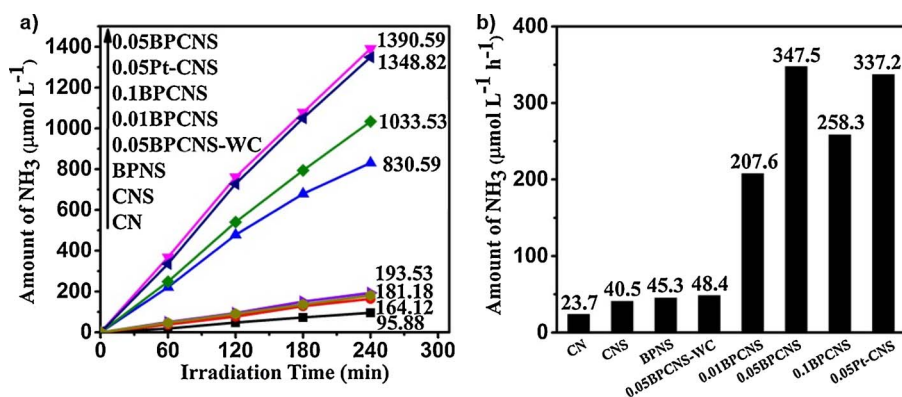
Fig. 2. a) Time course and b) 4-h average reaction rate of photocatalytic nitrogen fixation on CN, CNS, BPNS, 0.05BPCNS-WC and BPCNS.

experiment (Fig. 1d) revealed that the thickness of 0.05BPCNS was about 4–5 nm. The nitrogen adsorption–desorption isotherms and pore size distributions of CN, CNS, 0.05BPCNS were presented in Fig. 1e and f. Calculated by the Brunauer–Emmett–Teller (BET) function, the specific surface area of CN, CNS, 0.05BPCNS were 5.9 m^2 g^{-1}, 62.2 m^2 g^{-1}, and 51.8 m^2 g^{-1}, respectively. In addition, these photocatalysts exhibited a very broad pore size distribution in the 1–62 nm region, due to the aggregation during the synthesis process.

The visible-light photocatalytic nitrogen fixation activities of photocatalysts with different BPNS contents are shown in Fig. 2. The nitrogen fixation rates of CN (23.7 μmol L^{-1} h^{-1}), CNS (40.5 μmol L^{-1} h^{-1}), BPNS (45.3 μmol L^{-1} h^{-1}) and 0.05BPCNS-WC (48.4 μmol L^{-1} h^{-1}) are similar, while BPCNS exhibited a much improved photocatalytic activity for nitrogen fixation compared to either BPNS or CNS. The highest photocatalytic rate for nitrogen fixation is observed on 0.05BPCNS (347.5 μmol L^{-1} h^{-1}), which is even higher than that on 0.05Pt-CNS (337.2 μmol L^{-1} h^{-1}, a series of experiments were performed to determine the optimal amount of Pt as shown in Fig. S3). However, the nitrogen fixation rate decreased to 258.3 μmol L^{-1} h^{-1} when the BP content increased to 10%, which may be attributed to an increase in the recombination of charge carriers owing to the excessive loading of the cocatalyst [29]. Similar results are demonstrated through the photocatalytic reduction of Cr(VI) under visible light irradiation. It can be clearly seen that the reduction activity decreases in the order 0.05BPCNS > 0.1BPCNS > 0.01BPCNS > 0.05Pt-CNS > 0.05BPCNS-WC > CNS > CN (Fig. S4). Both the above experiments prove the high activity of BPCNS for nitrogen fixation as well as pollutant reduction.

XPS is performed to analyze the chemical structure and electron distribution of the photocatalysts. Based on the high resolution N 1 s XPS spectra (Fig. 3a), there are three types of N species in CNS and 0.05BPCNS. The peaks centered at 398.53, 400.37, and 404.45 eV can be assigned to the sp2 nitrogen (C−N=C), tertiary N (C$_3$−N or C−N−H), and π-excitation, respectively. The N 1 s spectrum of CNS is almost the same as that of 0.05BPCNS, indicating that there is no significant difference in N species between CNS and 0.05BPCNS. As shown in Fig. 3b, the peak at 284.60 eV is ascribed to graphitic carbon (C=C) as a reference to calibrate binding energies, and the peak at 287.99 eV corresponds to sp2C in the heptazine units [5]. The P 2p spectrum of the BPNS (Fig. 3c) can be deconvoluted into three peaks at 129.94, 130.76, and 134.35 eV, which are attributed to P 2p3/2, P 2p1/2, and P$_x$O$_y$, respectively [30]. The spectrum of 0.05BPCNS shows a much stronger P$_x$O$_y$ peak compared with the BPNS; this may be caused by the partial oxidation of BP during the preparation process. It is worth noting that the peaks of both P 2p3/2 and P 2p1/2 for BPCNS shift towards lower binding energies, while the peak of sp2C shifts towards a higher binding energy relative to the BPNS and CNS. These shifts may be caused by a partial electron transfer from the electron-rich CNS to the BPNS. The electron transfer decreases the outer electron density of the C atoms and weakens the shielding effect on the inner layer

electrons, resulting in an increase in the binding energy of sp2C [31]. Meanwhile, the electron density of the P atoms increases, which causes the decrease in the binding energies of P 2p3/2 and P 2p1/2. Based on these results, it is reasonable to suspect that a strong covalent bond between sp2C and P is formed during the synthesis process of 0.05BPCNS, which causes redistribution of the electron densities of C and P atoms.

Fig. 3d shows a comparison of the FTIR spectra of BPCNS, CN, and CNS. All of the samples exhibit bands at 1200–1600 cm^{-1}, which correspond to the typical stretching vibrational modes of heptazine-derived repeating units. Besides, the characteristic breathing mode of triazine units at 806 cm^{-1} is observed [28]. This suggests that neither the exfoliation of CN nor the combination with BPNS alter the chemical structure of CN.

^{31}P solid-state NMR was performed to investigate the chemical state of phosphorus atoms in BP and 0.05BPCNS. As presented in Fig. 3e, only one peak at 20.29 ppm can be observed in the spectrum of BP, which is the characteristic peak of BP. With regard to the spectrum of 0.05BPCNS, three peaks with chemical shifts centered at 19.20, 0.06, and −11.09 ppm can be observed, which correspond to the P atoms in BP, those in P$_x$O$_y$, and those bonded with C atoms, respectively [32]. No peak at −11.09 ppm can be observed in the ^{31}P NMR spectrum of 0.05BPCNS-WC (Fig. S5), indicating that there is no C−P bond between BP and CNS in 0.05BPCNS-WC. The formation of P$_x$O$_y$ is inevitable during the synthesis of 0.05BPCNS. It is notable that the peak of BP in the spectrum of 0.05BPCNS shifts towards a high field compared with that in the spectrum bulk BP, which suggests the redistribution of the electron densities of P atoms in 0.05BPCNS.

The photoelectrochemical properties of CN, CNS, and BPCNS are researched through UV–vis DRS, VBXPS, Mott–Schottky curves, EPR, PL, time-resolved fluorescence, and photocurrent transient response analysis. The UV–vis DRS spectra of CN, CNS, and BPCNS are presented in Fig. 4a. CNS exhibits a blue shift in the adsorption edge compared with CN due to the quantum size effect. Besides, the UV–vis DRS spectrum of 0.05BPCNS-WC (Fig. S5) is similar to that of 0.05BPCNS. The corresponding band gaps of the photocatalysts were determined using the Kubelka–Munk function (Fig. 4b) [33]. The band gaps of CNS and 0.05BPCNS are 2.92 and 2.87 eV, respectively. According to the VBXPS results (Fig. 4c), the VB potentials of 0.05BPCNS and CNS are found to be 1.57 and 1.79 eV, respectively. By combining with the UV–vis DRS results, the CB potentials of BPCNS and CNS are calculated to be −1.32 and −1.13 eV, respectively. As is well known, CN is a π-conjugated organic semiconductor, and its VB and CB potential can be modified by C$_{60}$ or CoP according to the related research [13,26]. The CB potential of BPCNS is more negative than that of CNS, indicating that the photogenerated electrons of BPCNS may have better reduction ability than those of CNS. This may be one of the reasons for the enhanced nitrogen fixation efficiency of BPCNS.

Mott–Schottky experiments are performed to determine the flat band potential (E$_{fb}$) and estimate the donor concentration (N$_D$). Fig. 4d
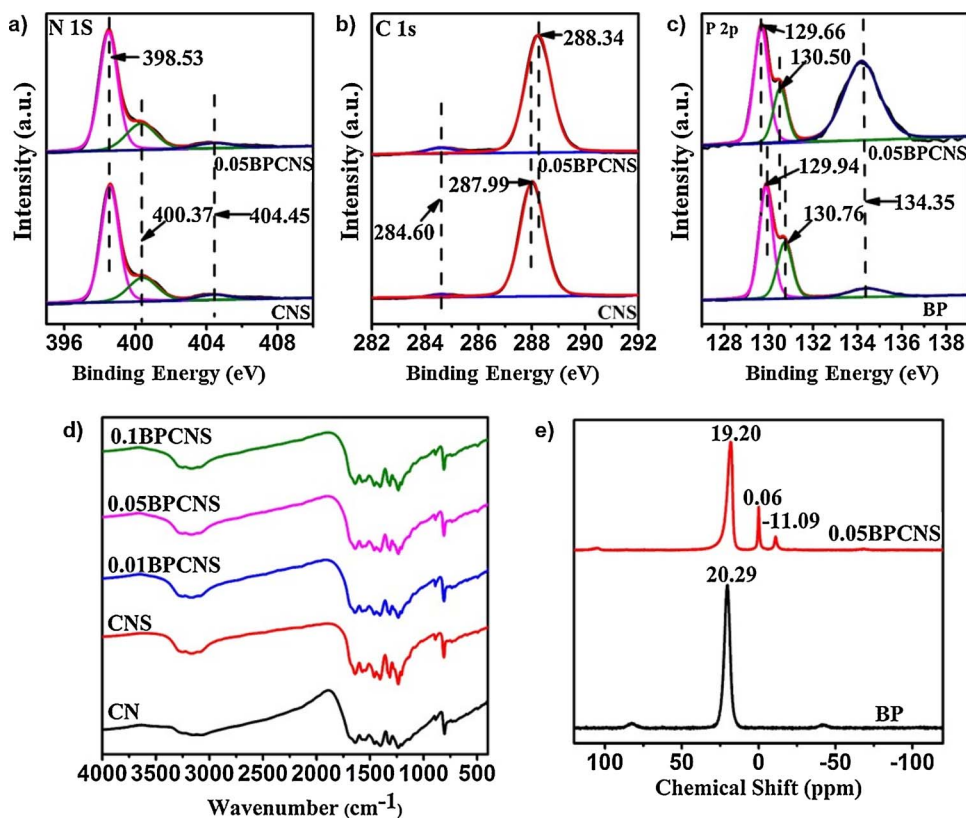
Fig. 3. XPS spectra of a) N1s and b) C1s in CNS and 0.05BPCNS. XPS spectra of c) P2p in BP and 0.05BPCNS. d) The FTIR spectra of CN, CNS, and BPCNS. e) The ^{31}P NMR spectra of BP and 0.05BPCNS.

presents the Mott–Schottky plots obtained from CNS and 0.05BPCNS in 0.1 M Na$_2$SO$_4$ solution. E$_{fb}$ can be estimated from the intercept on the x-axis by extrapolating the Mott–Schottky plot. In this case, the E$_{fb}$ values of CNS and 0.05BPCNS are −1.31 and −1.12 eV, respectively.

Normally, the value of E$_{fb}$ can be considered as the position of the CB (E$_{CB}$). In this system, these E$_{CB}$ values are in good agreement with the results calculated from the UV–vis DRS and VBXPS results mentioned above. The carrier density (N$_D$) can also be estimated from
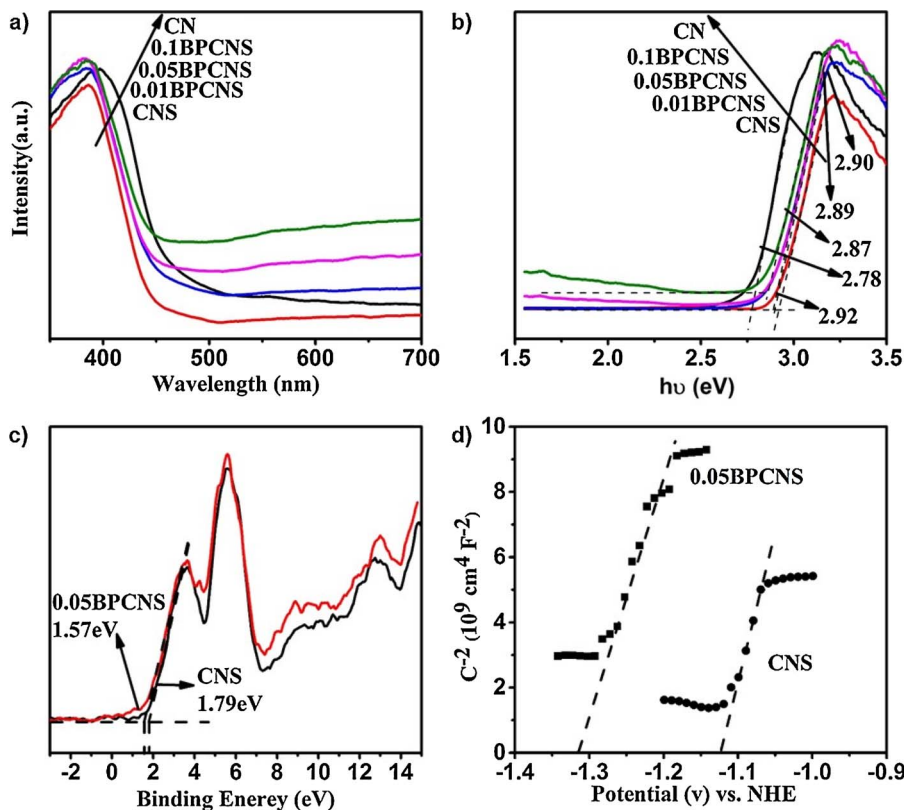

Fig. 4. a) UV–vis DRS spectra and b) Kubelka–Munk plots converted from the UV–vis DRS spectra of CN, CNS, and BPCNS. c) VBXPS spectra and d) Mott-Schottky plots of CNS and 0.05BPCNS.
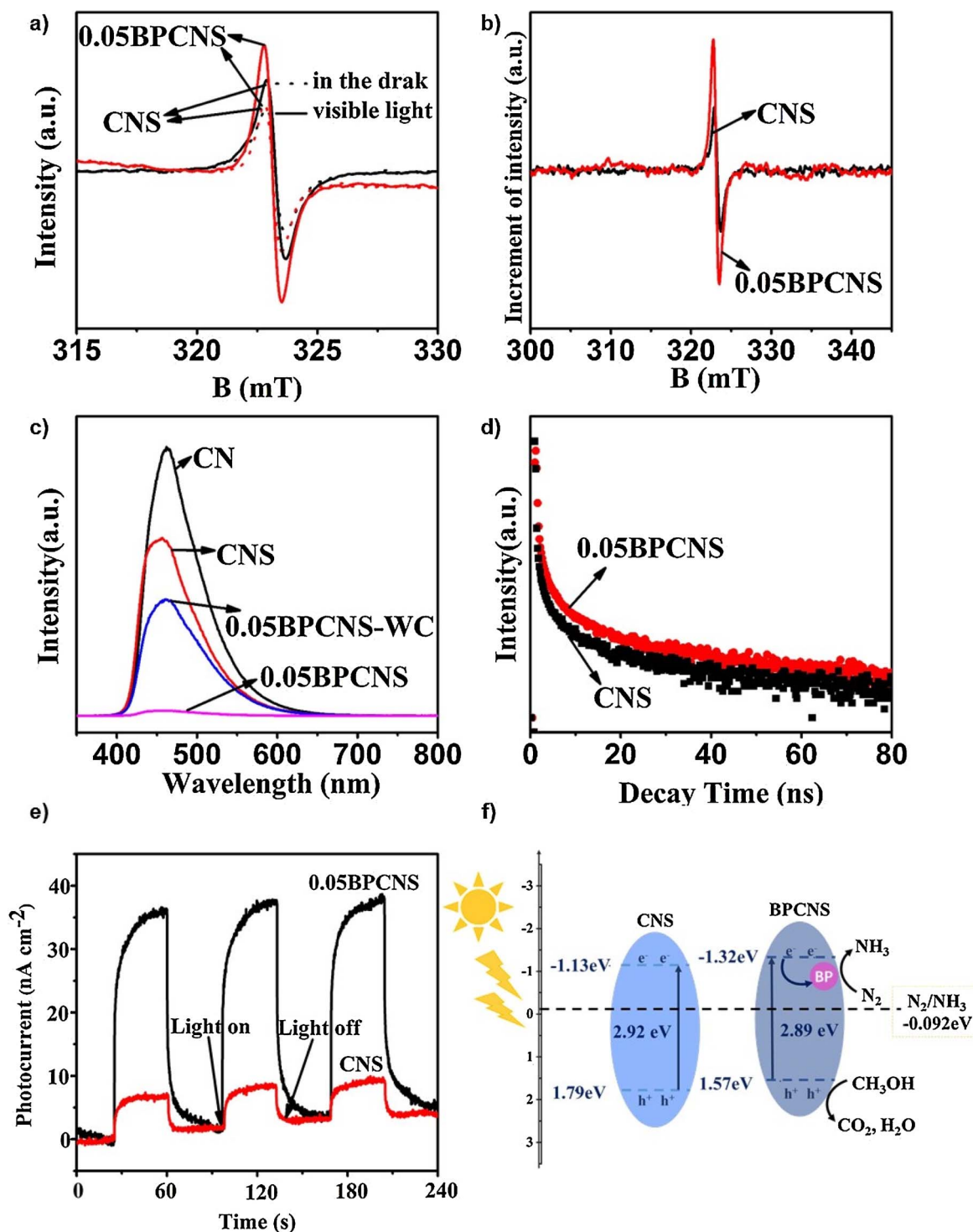
Fig. 5. a) EPR spectra CNS and 0.05BPCNS and b) corresponding increment of intensity under visible light irradiation. c) PL spectra of CN, CNS, 0.05BPCNS and 0.05BPCNS-WC. d) Time-resolved fluorescence spectra of CNS and 0.05BPCNS. e) Transient photocurrent response for CNS and 0.05BPCNS. f) The possible photocatalytic nitrogen fixation mechanism over 0.05BPCNS.

Mott–Schottky plots with Eqs. (1) and (2) [34]:

$$\frac{1}{C^2} = \frac{2}{e\varepsilon\varepsilon_o N_D}\left(E - E_{fb} - \frac{\kappa T}{e}\right) \tag{1}$$

$$N_D = \frac{2}{e\varepsilon\varepsilon_0}\left[\frac{d\left(\frac{1}{C^2}\right)}{d(E)}\right]^{-1} \tag{2}$$

where C is the capacitance of the space charge layer; ε is the dielectric

constant (15.6 for CN); ε_0 is the vacuum permittivity (8.85×10^{-14} F cm^{-1}); E is the potential versus the normal hydrogen electrode; κ is the Boltzmann constant (1.38×10^{-23} J K^{-1}); e is the electron charge (1.602×10^{-19} C). The N_D values of CNS and 0.05BPCNS are calculated to be 2.49×10^{19} and 3.81×10^{19} cm^{-3}, respectively, suggesting that the electron transfer efficiency is improved in 0.05BPCNS [34].

EPR is conducted to detect the spin state of unpaired electrons. As shown in Fig. 5a and b, CN exhibits a single Lorentzian line with a g
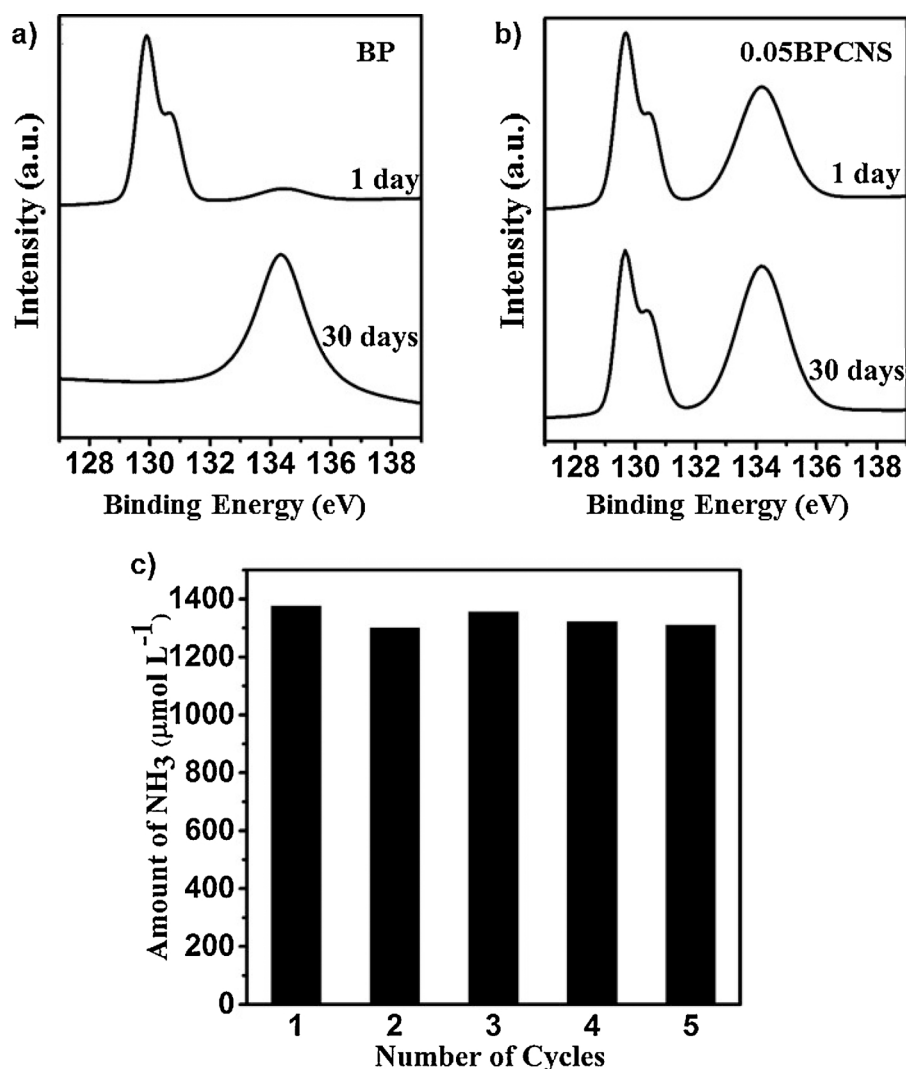
Fig. 6. P2p XPS spectra of a) BP and b) 0.05BPCNS. c) Recycle runs of nitrogen fixation on 0.05BPCNS. The sampling time was 4 h after irradiation.

factor of 2.003 due to the unpaired electron of the π-bonded aromatic rings. BPCNS exhibits a similar peak intensity compared with CNS in the dark, while BPCNS shows a much higher increment in peak intensity under visible light irradiation, which indicates that the electrons in BPCNS are inclined to be excited due to the change in the π-conjugate system of CN caused by the formation of C−P bonds [35].

Fig. 5c presents the PL spectra for CN, CNS, 0.05BPCNS-WC, and 0.05BPCNS at an excitation wavelength of 330 nm. The emission peak of CN is centered at 465 nm and is attributed to the recombination of holes and electrons in the valence and conduction bands. The 0.05BPCNS exhibits a much lower emission peak than 0.05BPCNS-WC, implying that the recombination of photogenerated charge carriers is inhibited owing to the efficient transfer of photogenerated electrons via C−P bonds. The same results can be obtained from time-resolved fluorescence spectra. As shown in Fig. 5d, the fluorescence lifetime of BPCNS (15.31 ns) is longer than the others, which suggested the effective transfer of photogenerated electrons to BP.

In addition, the photocurrent transient response is conducted to explore the generating and transferring efficiency of the photogenerated charge carriers under irradiation [36]. Fig. 5e compares the photocurrent transient responses of CNS and 0.05BPCNS coated on ITO electrodes during several on-off cycles. 0.05BPCNS shows a higher current density than CNS under irradiation with good reversibility, which may be explained according to two aspects: (1) the separation of photogenerated electrons and holes is improved due to the effective electron transfer through the B−P bond in BPCNS; (2) more electrons

can be excited in BPCNS under irradiation owing to the enhanced light harvesting ability. EIS was also measured and presented in Fig. S7. The smaller arc radius on the EIS Nyquist plot of 0.05BPCNS suggests that faster interfacial charge transfer is found due to the participation of BP. Fig. S8 shows the linear sweep voltammetry (LSV) curves of GCE modified with CNS and 0.05BPCNS. The observed current in the range of 0 to −1.0 V versus Ag/AgCl can be ascribed to the reduction reaction [37]. 0.05BPCNS showed a much higher activity compared with CNS, which indicated that BPNS could efficiently enhance the reduction capacity of photocatalyst.

Based on the above results, the enhancement of reduction activity on 0.05BPCNS can be explained as follows (Fig. 5f). Firstly, the C−P covalent bonds in 0.05BPCNS formed between BP and CNS accelerate the electron transfer and improve the separation of photogenerated charge carriers. Secondly, the formation of C−P bonds leads to rearrangement of the electrons on neighboring P and C atoms in BPNS and CNS. Thus, P atoms with more electrons in C−P bonds can act as the electron donors in the 0.05BPCNS photocatalyst. Thirdly, the stable π-conjugate system of CNS is changed by C−P bonds, which is conducive to the excitation of electrons in the photocatalyst. Finally, the CB potential of 0.05BPCNS is 0.19 eV negative than that of CNS, suggesting that the photogenerated electrons of 0.05BPCNS are more reductive. The electrons in the VB are excited to the CB under irradiation and transferred to BPNS via C−P bonds. The nitrogen adsorbed on the surface of BP reacts with the photogenerated electrons to form NH_3, which finally dissolves in water as NH_4^+.

Stability is also an important factor in evaluating the performance of a photocatalyst. It is demonstrated that BP is highly active to oxygen due to the lone pair electrons on phosphorus atom. BP will continue to be oxidized until it is completely etched away due to the dissolution of surface P_xO_y in water [22]. Fig. 6a shows the P 2p XPS spectra of BP exposed in air after 1 day and 30 days. As mentioned before, the peaks at 129.94 and 130.76 eV are ascribed to BP and the peak at 134.45 eV is assigned to P_xO_y. Only a small part of BP is oxidized to P_xO_y after 1 day. However, BP is completely transformed to P_xO_y after 30 days. The P 2p XPS spectra of 0.05BPCNS exposed to air after 1 day and 30 days are presented in Fig. 6b. The formation of P_xO_y during the synthesis of xBPCNS is inevitable. Surprisingly, the peak for P_xO_y increases only slightly after 30 days, with strong peaks for BP showing in the spectrum, which indicates that the stability of BP is significantly enhanced in the composition. As reported, BP is easily oxidized due to the lone pairs, while the lone pairs in BP can form stable C−P bonds by reacting with the C atoms in 0.05BPCNS to reduce the number of oxidation sites. A similar method was reported by Zhao et al. The formation of stable Ti−P bonds was achieved by the reaction between titanium sulfonate and BP, and the obtained catalyst showed high efficiency and stability [38]. Fig. 6c shows the cycling experiment for visible-light photocatalytic nitrogen fixation over 0.05BPCNS. The catalyst can maintain an efficient and durable photocatalytic performance after five repeated runs.

4. Conclusion

A metal-free black phosphorus nanosheets decorated graphitic carbon nitride nanosheets photocatalyst (BPCNS) is successfully synthesized. BPCNS exhibits high activities in both photocatalytic nitrogen fixation and Cr(VI) reduction with BP acting as the cocatalyst. The photocatalytic nitrogen fixation rate of 0.05BPCNS ($347.5\,\mu mol\,L^{-1}\,h^{-1}$) is 8.6 times as high as that of CNS ($40.5\,\mu mol\,L^{-1}\,h^{-1}$). The photocatalytic reduction performance of 0.05BPCNS is even better than that of the traditional Pt loaded CNS photocatalyst. The C−P bonds in 0.05BPCNS play an important role in the improvement of photocatalytic activity. The electrons in 0.05BPCNS are more likely to be excited due to the change in the π-conjugate system of graphitic carbon nitride caused by the formation of C−P bonds. The recombination of photogenerated charge carriers is inhibited owing to the efficient transfer of photogenerated electrons via C−P bonds. Furthermore, the formation of C−P bonds in 0.05BPCNS occupies some of the lone pairs on P atoms and inhibits the oxidation of BP by reducing the number of oxygen reactive sites. 0.05BPCNS retains the same chemical structure after exposure to air for 30 days. No significant deterioration was observed in the photocatalytic nitrogen fixation activity of 0.05BPCNS after five cycles. This work presents a significant step in developing an efficient multifunctional photocatalyst using low cost elements (C, N, and P) that are abundant in nature.

Acknowledgements

Appendix A. Supplementary data

Supplementary data associated with this article can be found, in the online version, at http://dx.doi.org/10.1016/j.apcatb.2017.09.010.

References

[1] P.C. Dos Santos, R.Y. Igarashi, H. Lee, B.M. Hoffman, L.C. Seefeldt, D.R. Dean, Substrate interactions with the nitrogenase active site, Acc. Chem. Res. 38 (2005) 208–214.

[2] A. Banerjee, B.D. Yuhas, E.A. Margulies, Y. Zhang, Y. Shim, M.R. Wasielewski, M.G. Kanatzidis, Photochemical nitrogen conversion to ammonia in ambient conditions with FeMoS–chalcogels, J. Am. Chem. Soc. 137 (2015) 2030–2034.

[3] Y. Nishibayashi, M. Saito, S. Uemura, S. Takekuma, H. Takekuma, Z. Yoshida, Buckminsterfullerenes: a non-metal system for nitrogen fixation, Nature 428 (2004) 279–280.

[4] X. Wang, K. Maeda, A. Thomas, K. Takanabe, G. Xin, J.M. Carlsson, K. Domen, M. Antoietti, A metal-free polymeric photocatalyst for hydrogen production from water under visible light, Nat. Mater. 8 (2009) 76–80.

[5] Y. Wang, X. Wang, M. Antonietti, Polymeric graphitic carbon nitride as a heterogeneous organocatalyst: from photochemistry to multipurpose catalysis to sustainable chemistry, Angew. Chem. Int. Ed. 51 (2012) 68–89.

[6] J. Zhang, X. Chen, K. Takanabe, K. Maeda, K. Domen, J.D. Epping, X. Fu, M. Antonietti, X. Wang, Synthesis of a carbon nitride structure for visible-light catalysis by copolymerization, Angew. Chem. Int. Ed. 49 (2010) 441–444.

[7] N. Cheng, J. Tian, Q. Liu, C. Ge, A.H. Qusti, A.M. Asiri, A.O. Al-Youbi, X. Sun, Au–nanoparticle–loaded graphitic carbon nitride nanosheets: green photocatalytic synthesis and application toward the degradation of organic pollutants, ACS Appl. Mater. Inter. 5 (2013) 6815–6819.

[8] S. Samanta, S. Martha, K. Parida, Facile synthesis of Au/g-C$_3$N$_4$ nanocomposites: an inorganic/organic hybrid plasmonic photocatalyst with enhanced hydrogen gas evolution under visible-light irradiation, Chemcatchem. 6 (2014) 1453–1462.

[9] L. Ge, C. Han, J. Liu, Y. Li, Enhanced visible light photocatalytic activity of novel polymeric g-C$_3$N$_4$ loaded with Ag nanoparticles, Appl. Catal. A Gen. 215 (2011) 409–410.

[10] X. Li, W. Bi, L. Zhang, S. Tao, W. Chu, Q. Zhang, Y. Luo, C. Wu, Y. Xie, Single-atom Pt as Co-catalyst for enhanced photocatalytic H$_2$ evolution, Adv. Mater. 28 (2016) 2427–2431.

[11] C. Chang, M. Fu, C. Wang, G. Shan, L. Zhu, Photodegradation of bisphenol A by highly stable palladium-doped mesoporous graphite carbon nitride (Pd/mpg-C$_3$N$_4$) under simulated solar light irradiation, Appl. Catal. B Environ. 142 (2013) 553–560.

[12] J. Liu, Y. Liu, N. Liu, Y. Han, X. Zhang, H. Huang, Y. Lifshitz, S.-T. Lee, J. Zhong, Z. Kang, Metal-free efficient photocatalyst for stable visible water splitting via a two-electron pathway, Science 347 (2015) 970–974.

[13] W. Wang, J.C. Yu, D. Xia, P. Wong, Y. Li, Graphene and g-C$_3$N$_4$ nanosheets cowrapped elemental α–sulfur as a novel metal-free heterojunction photocatalyst for bacterial inactivation under visible-light, Environ. Sci. Technol. 47 (2013) 8724–8732.

[14] A. Suryawanshi, P. Dhanasekaran, D. Mhamane, S. Kelkar, S. Patil, N. Gupta, S. Ogale, Doubling of photocatalytic H$_2$ evolution from g–C$_3$N$_4$ via its nanocomposite formation with multiwall carbon nanotubes: electronic and morphological effects, Int. J. Hydrogen Energy 37 (2012) 9584–9589.

[15] X. Bai, L. Wang, Y. Wang, W. Yao, Y. Zhu, Enhanced oxidation ability of g-C$_3$N$_4$ photocatalyst via C$_{60}$ modification, Appl. Catal. B Environ. 152 (2014) 262–270.

[16] T. Nilges, M. Kersting, T. Pfeifer, A fast low-pressure transport route to large black phosphorus single crystals, J. Solid State Chem. 181 (2008) 1707–1711.

[17] M.Z. Rahman, C. Kwong, K. Davey, S. Qiao, 2D phosphorene as a water splitting photocatalyst: fundamentals to applications, Energy Environ. Sci. 9 (2016) 709–728.

[18] L. Li, Y. Yu, G. Ye, Q. Ge, X. Ou, H. Wu, D. Feng, X. Chen, Y. Zhang, Black phosphorus field-effect transistors, Nat. Nanotechnol. 9 (2014) 372–377.

[19] J. Sun, G. Zheng, H.-W. Lee, N. Liu, H. Wang, H. Yao, W. Yang, Y. Cui, Formation of stable phosphoruscarbon bond for enhanced performance in black phosphorus nanoparticle-graphite composite battery anodes, Nano. Lett. 14 (2014) 4573–4580.

[20] L. Kou, T. Frauenheim, C. Chen, Phosphorene: fabrication, properties, and applications, J. Phys. Chem. Lett. 6 (2015) 2794–2805.

[21] J. Dai, X. Zeng, Bilayer phosphorene: effect of stacking order on bandgap and its potential applications in thin-film solar cells, J. Phys. Chem. Lett. 5 (2014) 1289–1293.

[22] C. Hao, B. Yang, F. Wen, J. Xiang, L. Li, W. Wang, Z. Zeng, B. Xu, Z. Zhao, Z. Liu, Y. Tian, Flexible all-solid-state supercapacitors based on liquid-exfoliated black-phosphorus nanoflakes, Adv. Mater. 28 (2016) 3194–3201.

[23] H. Lee, S. Lee, J. Won, B.-C. Son, S. Choi, Y. Kim, S. Park, H.-S. Kim, Y.-C. Lee, J. Lee, Stable semiconductor black phosphorus (BP)@ titanium dioxide (TiO$_2$) hybrid photocatalysts, Sci. Rep. 5 (2015) 8691.

[24] Z. Shen, S. Sun, W. Wang, J. Liu, Z. Liu, J.C. Yu, A black-red phosphorus heterostructure for efficient visible-light-driven photocatalysis, J. Mater. Chem. A 3 (2015) 3285–3288.

[25] G. Wu, K. More, C.M. Johnston, P. Zelenay, High-performance electrocatalysts for oxygen reduction derived from polyaniline, iron, and cobalt, Science 332 (2011) 443–447.

[26] C. Li, Y. Du, D. Wang, S. Yin, W. Tu, Z. Chen, M. Kraft, G. Chen, R. Xu, Unique PCoN surface bonding states constructed on g-C$_3$N$_4$ nanosheets for drastically enhanced photocatalytic activity of H$_2$ evolution, Adv. Funct. Mater. 27 (2017) 1604328.

[27] M.C. Stan, J. von Zamory, S. Passerini, T. Nilges, M. Winter, Puzzling out the origin of the electrochemical activity of black P as a negative electrode material for lithium-ion batteries, J. Mater. Chem. A 1 (2013) 5293–5300.

[28] P. Niu, L. Zhang, G. Liu, H. Cheng, Graphene-like carbon nitride nanosheets for improved photocatalytic activities, Adv. Funct. Mater. 22 (2012) 4763–4770.

[29] J. Ran, J. Zhang, J. Yu, M. Jaroniec, S. Qiao, Earth-abundant cocatalysts for semiconductor-based photocatalytic water splitting, Chem. Soc. Rev. 43 (2014) 7787–7812.

[30] X. Zhang, H. Xie, Z. Liu, C. Tan, Z. Luo, H. Li, J. Lin, L. Sun, W. Chen, Z. Xu, L. Xie, W. Huang, H. Zhang, Black phosphorus quantum dots, Angew. Chem. Int. Ed. 54 (2015) 3653–3657.

[31] O. Park, Y. Kang, Preparation and characterization of silica-coated TiO_2 nano-particle, Colloids Surf. A 257 (2005) 261–265.

[32] S. Lange, P. Schmidt, T. Nilges, Au_3SnP_7@black phosphorus: an easy access to black phosphorus, Inorg. Chem. 46 (2007) 4028–4035.

[33] Z. Zou, J. Ye, K. Sayama, H. Arakawa, Direct splitting of water under visible light irradiation with an oxide semiconductor photocatalyst, Nature 414 (2001) 625–627.

[34] Y. Liu, L. Liang, C. Xiao, X. Hua, Z. Li, B. Pan, Y. Xie, Promoting photogenerated holes utilization in por-rich WO_3 ultrathin nanosheets for efficient oxygen-evolving photoanode, Adv. Energy. Mater. 6 (2016) 1600437.

[35] J. Zhang, M. Zhang, S. Lin, X. Fu, X. Wang, Molecular doping of carbon nitride photocatalysts with tunable bandgap and enhanced activity, J.Catal. 310 (2014) 24–30.

[36] Z. Huang, Q. Sun, K. Lv, Z. Zhang, M. Li, B. Li, Effect of contact interface between TiO2 and g-C_3N_4 on the photoreactivity of g-C_3N_4/TiO_2 photocatalyst: (001) vs (101) facets of TiO_2, Appl. Catal. B Environ. 164 (2015) 420–427.

[37] Y. Hou, A.B. Laursen, J. Zhang, G. Zhang, Y. Zhu, X. Wang, S. Dahl, I. Chorkendorff, Layered nanojunctions for hydrogen-evolution catalysis, Angew. Chem. Int. Ed. 52 (2013) 3621–3625.

[38] Y. Zhao, H. Wang, H. Huang, Q. Xiao, Y. Xu, Z. Gao, H. Xie, J. Shao, Z. Sun, W. Han, X.-F. Yu, P. Li, P.K. Chu, Surface coordination of black phosphorus for robust air and water stability, Angew. Chem. Int. Ed. 55 (2016) 5003–5007.